Geometry and topology of fracture systems

1997 J. Phys. A: Math. Gen. 30 1415

(http://iopscience.iop.org/0305-4470/30/5/012)

J. Phys. A: Math. Gen. **30** (1997) 1415–1444. Printed in the UK PII: S0305-4470(97)74526-8

Geometry and topology of fracture systems

O Huseby†‡, J-F Thovert† and P M Adler§

† LPTM, SP2MI, Bd 3, Téléport 2, 86960 Futuroscope Cedex, France
‡ IFE, Instituttveien 18, PO Box 40, N-2007 Kjeller, Norway
§ IPGP, 4 Place Jussieu, Tour 14, 75252 Paris Cedex 05, France

Received 13 May 1996, in final form 7 October 1996

Abstract. Random three-dimensional fracture networks are generated according to various rules. Geometrical and topological features such as the number of three-dimensional blocks, the percolation thresholds and the cyclomatic numbers are studied with respect to fracture shapes and densities. All the results could be successfully interpreted by means of the excluded volume.

1. Introduction

Knowledge of geometrical properties of fracture networks is crucial to the understanding of flow and other transport processes in geological formations, both at small and large scales; the introduction of fractures in a porous rock matrix seriously alters the macroscopic properties of the formation. Moreover, studies of fracture geometries during the last 12–15 yr show that naturally occurring geological fractures exist on scales ranging from a few mm to several km (Sahimi and Yortsos, 1990). Therefore, fracture networks are likely to influence the transports on a large range of scales. Because of their importance, fracture networks are studied and applied in various areas such as oil and gas recovery, hydrology, nuclear waste storage and geothermal energy exploitation.

Geological fractures can be defined as discrete discontinuities within a rock mass; these breaks are characterized by the fact that their local aperture (defined as the local distance between the two surfaces which limit the fracture) is significantly smaller than their lateral extent; in other words, when they are viewed from far away, fractures can be assimilated to surfaces of discontinuity; in most cases, these surfaces are relatively level. Fractures have varying degrees of aperture, and may in some cases be completely closed either because of deposition of material induced by fluid flow, or by displacements of the matrix.

An important specialized literature has been devoted to the different task of collecting relevant data and to analyse them. It would be too lengthy to detail it and we shall content ourselves with the recent general reference of Cowie *et al* (1996). However, it should be noticed that the variety and the difficulty of getting real data stimulated the need for generating numerical fracture network models. General reviews on modelling can be found in chapter 7 of Sahimi (1995), Chiles (1988), Dershowitz and Einstein (1988), and Bear *et al* (1993).

The earliest fracture network models were deterministic because they are easier to treat theoretically, and because computer simulations can be done with low memory and short CPU time. Random network models are simplified if planar three-dimensional (3D) or linear two-dimensional (2D) fractures are assumed. Also, considering independent fracture

0305-4470/97/051415+30$19.50

location and orientations simplifies the models. When building numerical models, uniform distributions can be used as a starting point, and the relevant observed distributions of fracture lengths, orientation and location can easily be introduced later.

Some of the models discussed in the present work are inspired by 3D finite random disk models used by Andersson and Dverstop (1987) and Billaux *et al* (1989). In these models, fractures are represented in 3D by disks of finite radius. This assumption is supported by experimental observations that fractures are roughly disk shaped or elliptical (Pollard 1976). On the other hand, Gertsch (1995) gives an example where the fractures are far more complex than the simple disk picture.

For some applications, such as layered beds, hierarchical models may be of interest. Hierarchical models can be defined by using at least two families of fractures; the fractures of the second family are assumed to stop with a certain probability when they intersect a fracture of the first family. A hierarchical model has been considered by Lee *et al* (1990), where they extend a model introduced by Conrad and Jacquin (1975) and also by Acuna and Yortsos (1995).

Connectivity studies of fracture networks have been performed in 3D by Charlaix (1986). Moreover, Garborczi *et al* (1995) addressed the overlap of rotational ellipsoids in 3D, and gave results relevant for fracture networks. Connectivity in 2D was considered in Berkowitz (1995) among others. Balberg (1985) discussed universal percolation criteria and subsequently reviewed continuum percolation (Balberg, 1987).

Intersecting surfaces in 3D, and intersecting trace lines in 2D may constitute blocks (or areas in 2D) of the space, separated from the embedding space. Blocks in natural fracture networks are considered by Barthelemy (1992). A model to simulate key block size distributions is given by Mauldon (1995).

The general purpose of this work was to build general tools able to analyse the geometrical and the topological properties of random 3D fracture networks, whatever they are. The rest of this paper which gathers our results is organized as follows. In section 2, general assumptions concerning the models are given, followed by a description of each of them. In section 3, methods used to identify and characterize the fracture networks are presented. The topology of the fracture networks is addressed in section 4; three major sets of results are discussed, namely the partition of solid space into blocks, the percolating properties and the cyclomatic numbers of fracture networks. The physical motivations for the study of these quantities are briefly presented in each case.

2. Models

The medium is assumed to be spatially periodic at the large scale. A detailed description of spatially periodic media is given in Adler (1992), and only the main characteristics of these models are briefly repeated here. The geometrical and physical properties of the system under investigation are invariant under the translations

$$\boldsymbol{R}_{\boldsymbol{n}} = n_1\boldsymbol{l}_1 + n_2\boldsymbol{l}_2 + n_3\boldsymbol{l}_3 \tag{1}$$

where $\boldsymbol{n} = (n_1, n_2, n_3) \in \mathbb{Z}^3$, and where $\boldsymbol{l}_1$, $\boldsymbol{l}_2$ and $\boldsymbol{l}_3$ define a unit cell where the system is studied. The entire space is tiled by replicas of this unit cell, translated by $\boldsymbol{R}_{\boldsymbol{n}}$. All the studies presented in this paper are performed in cubic unit cells where $|\boldsymbol{l}_1| = |\boldsymbol{l}_2| = |\boldsymbol{l}_3| = L$. The assumption of spatially periodic media is important for the computations of the transport properties.

In order to represent a macroscopically homogeneous medium by a periodic model, one has to set the unit cell size much larger than any finite characteristic length scale in the

system. This restriction does not apply to model 2 described later, where one of the fracture families of the network is made of infinite parallel planes.

In all other cases, fractures are modelled as convex, finite polygons based on an embedding disk as shown in figure 1. The largest possible size of the polygon side is kept smaller than $L/2$, this is done by keeping the disk radius smaller than $L/4$. Hence, the situation displayed in figure 2(*b*) is avoided, where two homologous periodic copies of the same fracture 2 intersect fracture 1. This is simply a weak form of the general requirement that the unit cell size should be much larger than any local feature.

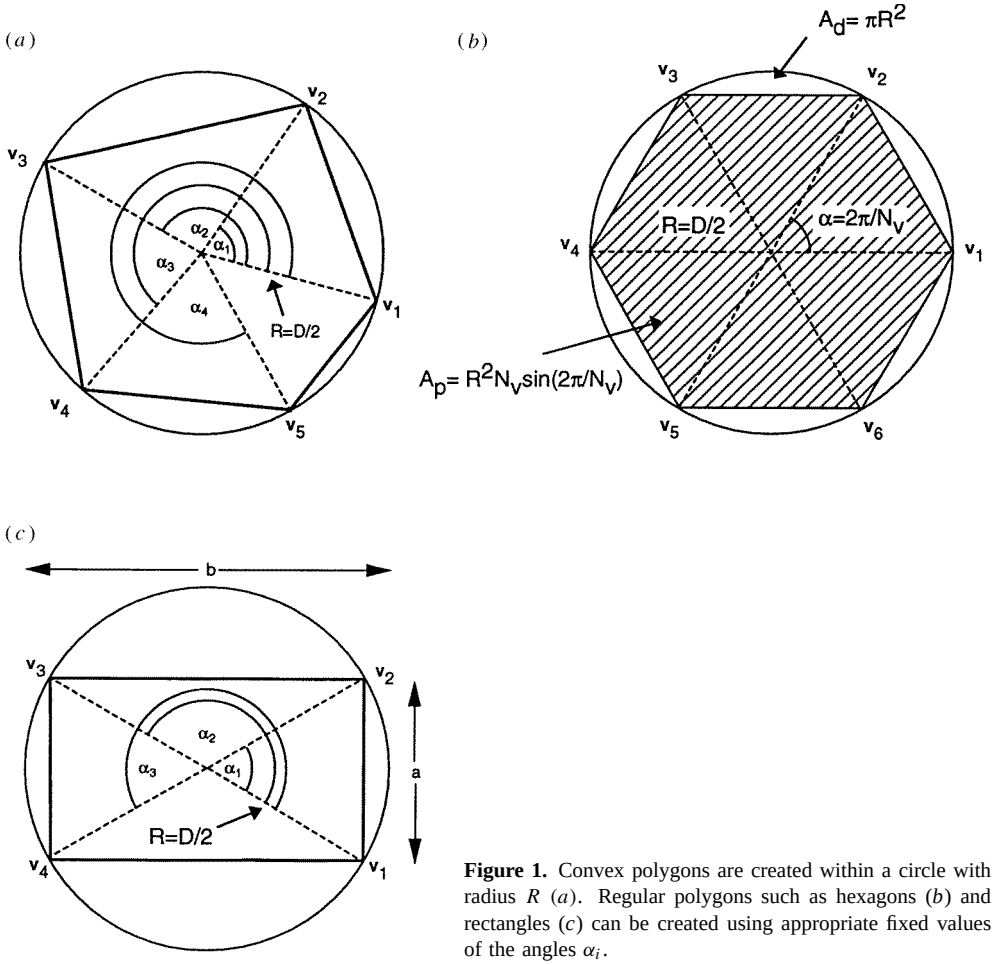

Figure 1. Convex polygons are created within a circle with radius R (*a*). Regular polygons such as hexagons (*b*) and rectangles (*c*) can be created using appropriate fixed values of the angles α_i.

The assumption of convex polygons is only a simplifying assumption. Real 3D fractures are generally not planar, as discussed by Gertsch (1995). However, this assumption provides a standard starting point for studying fracture networks. Convex polygons are fairly easy to treat numerically and they provide objects that can be used to analyse shape and area dependencies of geometrical and topological features in the fracture systems in a systematic manner.

Two additional general assumptions have been introduced. First, coplanar polygons cannot overlap. Second, only two polygons are assumed to intersect along a given line

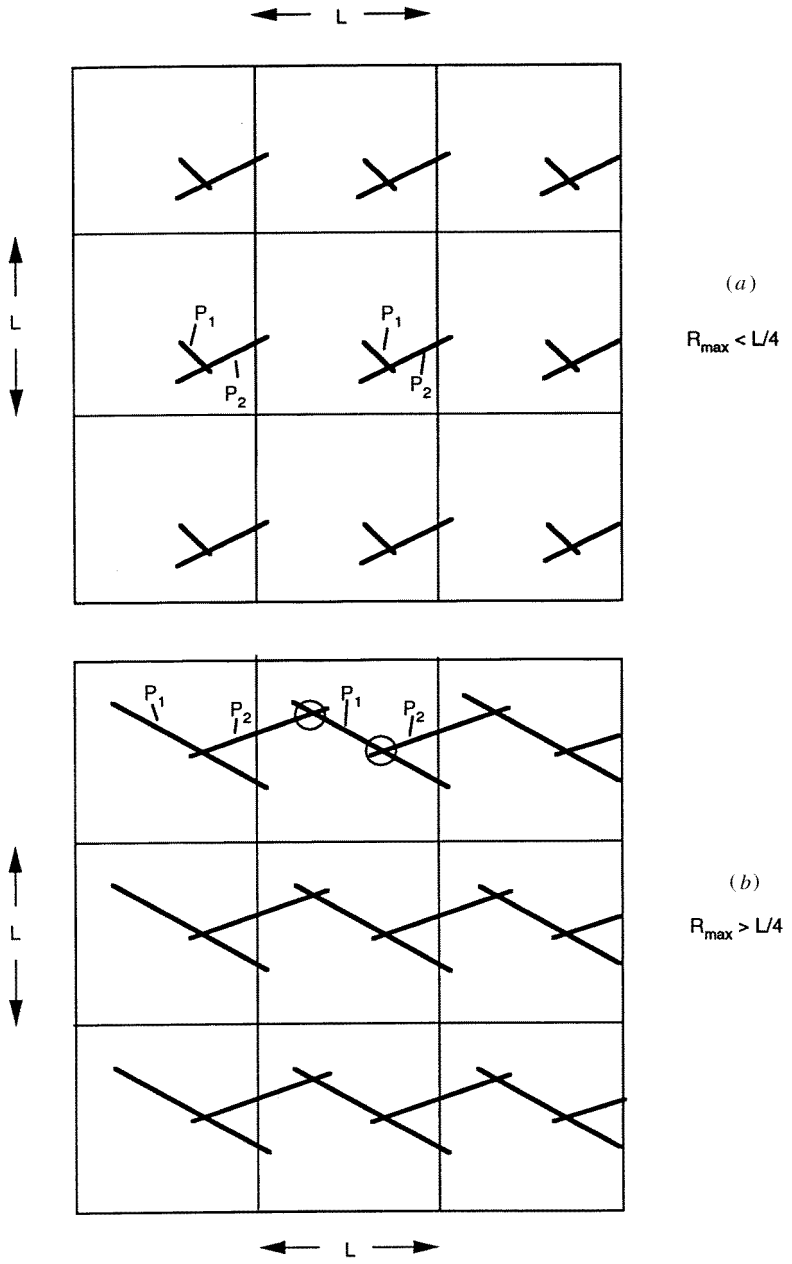

Figure 2. Two-dimensional illustration of fractures in a spatially periodic medium. When $R_{\max} < L/4$ (*a*), P_1 and P_2 have only one intersection in each unit cell. In contrast, when $R_{\max} > L/4$ (*b*) the polygons P_1 and P_2 can intersect twice.

segment. These two assumptions are employed because of the numerical and theoretical simplifications that they imply, but they are not expected to significantly influence the results, as can be seen by the following argument; working with real numbers, the probability that two polygons should have the same normal vectors by pure chance, is vanishingly small.

Also, the probability that two different intersection line segments overlap is negligible. Finally, two overlapping fractures can be viewed as a single one with a broader polygonal contour; it is handled by splitting it into convex parts.

The simplest model consists of a fracture network in which all fractures are created from disks whose centres are uniformly distributed within the unit cell. This implies that fractures may cross the imaginary unit cell boundaries, and reach the neighbouring cells of the periodic medium. The disk radii are chosen randomly from a uniform distribution $R \in [0, R_{\max}]$ where $R_{\max}$ is smaller than $L/4$ as explained above. A different size distribution, e.g. a lognormal distribution may easily be introduced at a later stage.

The directions of the fractures are given in terms of the normal vectors of the embedding planes. The normal vectors are uniformly distributed on the unit sphere. A preferred direction can be given to the family by distributing the normal vectors uniformly in a given solid angle centred around the average direction of the family. Again, a different distribution may be introduced at a later stage.

The number of corners (or vertices), N_v, of each fracture is chosen at random in the interval $[3, N_{\max}]$ with a uniform distribution; the vertices are distributed on the disk edge with angles $\alpha_1, \alpha_2, \ldots, \alpha_{N_v}$ which are uniformly distributed between 0 and 2π (see figure 1(*a*)).

This general definition can be simplified to yield networks of regular equal sized polygons. This is simply done by choosing $N_v > 3$ vertices, and N_v equal angles $\alpha_i = 2\pi/N_v$ as done in figure 1(*b*). Rectangles with ratios $a/b \neq 1$, where a and b are smallest and largest edge sizes respectively, are also readily obtained by a proper choice of angles (see figure 1(*c*)). This will be called model 1 in the following.

Other models are useful to consider briefly, though they are not systematically used here. They introduce some special features which introduce some additional difficulties. The second model is intended to reproduce hierarchical fracture networks, which are created from several families of fractures which appear successively. Such a hierarchy is introduced by generating a first family A, and then letting a second family B interact with the first one as it is created. A fracture P_B of the second family may stop at a fracture P_A of the first family. This generating procedure provides networks where T-shaped intersections are common. A flag is assigned to these intersections which are labelled, and can be treated specifically during the identification of blocks.

The third model is a special case of the second model, where an hierarchical network is created using two or more families of fractures. A first family A made of infinite parallel planes is generated. Since the medium is spatially periodic, the fractures of family A (or A-fractures) cross the entire unit cell.

Illustrations of three fracture systems, corresponding to models 1 and 3, are given in figure 3. Figure 3(*a*) corresponds to a number density of 2.29, which is close to the percolation threshold for this system (cf table 1). In figure 3(*b*), the shape of the polygons is randomized and the six vertices are randomly distributed around the circumventing disk. In figure 3(*c*), one realization of model 3 is displayed; the three infinite fractures span the unit cell of size $L = 12R$, where R is the size of the finite fractures (hexagons).

A large variety of networks can be generated by using these three basic models, whose systematic study would provide many novel results.

The present work is mostly focused on the methodology and to its application to the simplest version of model 1 where all polygons have the same shape and size. A systematic study was performed for the seven types of polygons listed in the first column of table 1; the number of sides is ranging from 3 (triangles) to 20; the list includes squares and rectangles.

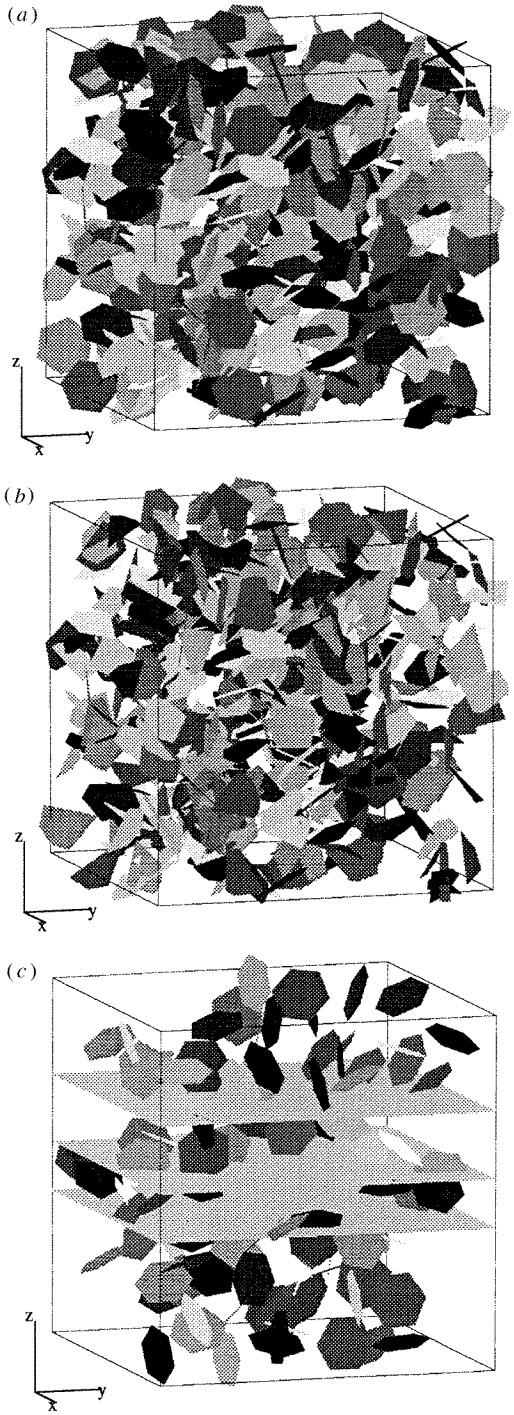

Figure 3. Realizations of the fracture models 1 and 3. In (*a*), model 1 was used to create a network containing 495 fractures of equal shape (hexagons) in a cell with size $L = 12R$. In (*b*), the network was created using hexagons with randomized angles. In (*c*), model 3 was used to create the network; three infinite fractures and 100 equal sized regular hexagons were used.

Table 1. Percolation thresholds and critical exponents for random fracture models.

Type of object	Percolation threshold $\rho_c(L \to \infty)$	Critical exponents ν	Linear correlation coefficients for ν	Linear correlation coefficients for ρ_c	ρ_c'
Equal sized Triangles	5.36 ± 0.01	0.991 ± 0.007	-0.9996	0.9657	2.26
Equal sized Squares	3.23 ± 0.01	1.029 ± 0.019	-0.9977	0.9583	2.28
Equal sized Hexagons	2.36 ± 0.01	1.055 ± 0.008	-0.9998	0.9995	2.30
Equal sized Octagons	2.09 ± 0.01	1.026 ± 0.025	-0.9986	0.9717	2.26
Equal sized 20-gons	1.89 ± 0.01	1.002 ± 0.014	-0.9995	0.9891	2.28
Equal sized Rectangles $a/b = \frac{1}{2}$	4.13 ± 0.02	0.967 ± 0.01	-0.9998	0.9246	2.22
Rectangles Unif. size dist. $a/b = \frac{1}{2}$	16.9 ± 0.2	0.87 ± 0.04	-0.9914	0.7725	2.24

3. Methods

The main tools needed to study the geometry and topology of the fracture network models defined above, are briefly described in this section.

The networks will be characterized by a graph which gives all the necessary relations and information. This graph, denoted by Γ_1, consists of *vertices* which correspond to the fracture polygons, and *edges* which correspond to the intersection between polygons. Γ_1 will be used to study network percolation as a function of fracture shape, distribution and density, as well as to characterize the topological features of the percolating components of the networks.

The second important concept is the one of blocks, which can be introduced as follows. The fractures create discontinuities in the solid matrix. A block is defined as a connected component of the solid matrix. In the second part of this section, it will be shown that the solid 3D blocks generated by the networks are identified with the help of a second graph Γ_2, whose vertices are the *elementary faces* of the polygons; edges relate vertices which correspond to two neighbouring, or *adjacent* elementary faces.

3.1. Fracture network

3.1.1. Intersection identification. Once the fractures have been generated by one of the schemes described in section 2, the polygon intersections and the intersection coordinates have to be determined. The procedure itself is geometric in character. It is not really difficult, but it is complex and thus costly in computing time. Moreover, the intersection test has to be performed for all pairs of polygons; hence, it involves about N^2 tests where N is the number of polygons.

The fracture networks are studied in a periodic medium as described in Adler (1992). Hence, in order to find intersections between two polygons pair P_{α_1} and P_{α_2}, periodic copies of one of the polygons have to be considered in the 26 neighbouring unit cells. However,

since the maximum size of the polygons is restricted to half the unit cell, they cannot cross simultaneously two opposite sides of the cell, and only eight periodic replicas have to be taken into account (e.g. the eight cells in contact with the front-top-left corner).

The information about the intersections is stored in the graph Γ_1 whose vertex v_α corresponds to polygon P_α and edge e_β to the intersection when it exists between two polygons P_{α_1} and P_{α_2} ($\alpha_1 < \alpha_2$); the edges are recursively numbered during the intersection procedure described above. Moreover, the respective position of the unit cells is stored in the triplet of flags $\boldsymbol{f}_\beta = (f_\beta^1, f_\beta^2, f_\beta^3)$; f_β^i is equal to 0 if the centres $\boldsymbol{r}_{\alpha_1}$ and $\boldsymbol{r}_{\alpha_2}$ of the circumventing disks of P_{α_1} and P_{α_2}, lie in the same unit cell, and ± 1 if $\boldsymbol{r}_{\alpha_2}$ is moved to $\boldsymbol{r}_{\alpha_2} \pm \boldsymbol{l}_i$ to find the intersection.

For the sake of clarity, let us consider the 2D example displayed in figure 4(*a*); in this case, $\boldsymbol{f}_\beta$ is reduced to a doublet (f_β^1, f_β^2). e_1 corresponds to the intersection between the two fractures P_1 (or v_1) and P_3 (or v_3); the fact that P_1 and P_3 intersect is stored as well as the intersection coordinates; the doublet of flags $\boldsymbol{f}_1$ relative to e_1 is obviously equal to (0,0). The fractures P_9 (or v_9) and P_1 (or v_1) also intersect at e_{11}; the doublet of flags $\boldsymbol{f}_{11}$ relative to e_{11} is now equal to $(-1, 0)$ according to the definition given in the previous paragraph.

Finally, the graph Γ_1 which corresponds to the network displayed in figure 4(*a*), is given in figure 4(*b*).

3.1.2. Connected and percolating components of Γ_1. Connectivity of Γ_1 is equivalent to the connectivity of the fracture networks which is one of the most important features we want to study. Two fractures P_i and P_j are said to belong to the same connected component if a path exists in Γ_1 from P_i to P_j. In figure 4(*b*), the network consists of two connected components denoted 1 and 2.

The connected components of Γ_1 are derived by a pseudo-diffusion algorithm, PERCOLA, described in Thovert *et al* (1993). It can be briefly described as follows. Define a discrete vector $M(i, t)$ with values 0 or 1 for each polygon P_i at time t; set $M(i, t)$ to 0 at $t = 0$, except for one polygon P_k. At each time step, $M(i, t + 1)$ is set to 1 for all the polygons which are neighbours of a polygon, P_j, where $M(j, t) = 1$ (figure 4(*c*)). After a certain number of time steps, the set $\{i : M(i, t/k) = 1\}$ is invariant, and corresponds to one connected component of Γ_1. This process can be repeated starting with a vertex which does not belong to the previous components until the set Γ_1 is exhausted.

The connected components of Γ_1 can be classified into percolating and non-percolating components. In a spatially periodic medium, a connected component is said to be percolating if it connects two opposite faces of the parallelepipedic unit cell, and if it contains two homologous fractures, i.e. two fractures with the same coordinates, modulo $\boldsymbol{R}_n$. Component 1 in figure 4(*b*) provides an example of a percolating component.

The diffusion algorithm PERCOLA can also be used to find the percolating connected components (cf Thovert *et al* 1993).

3.2. Solid blocks

As mentioned in the introduction of this section, the 3D solid blocks induced by the fracture networks are derived from a graph Γ_2 set up by the elementary faces of each polygon.

The physical idea which lies behind the algorithm, is relatively simple. A solid block is limited by several plane faces which are located within the construction polygons; to recognize such a block requires at least two steps, namely the recognition of the plane faces and the identification of faces which are neighbour one to another. A simple example is provided by a cube limited by six faces; each face is the neighbour of four others. Suppose that

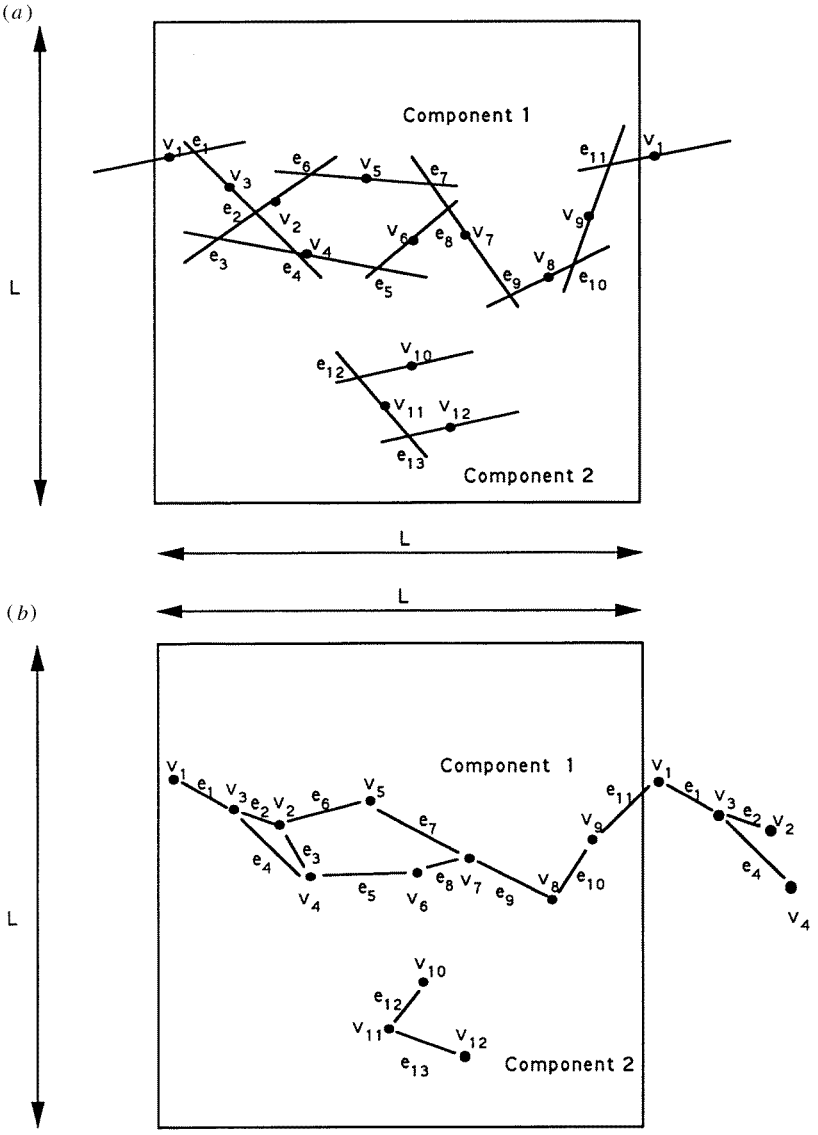

Figure 4. The graphs Γ_1 (b) for a 2D fracture network (a). The fracture P_α corresponds to the vertex v_α in the graph, and edges e_β connect vertices if the corresponding fractures intersect. Γ_1 has two connected components; 1 percolates through the cell, and 2 does not. Periodic conditions are used for component 1; v_1 is connected to v_3 in the unit cell (edge e_1), and to v_9 through the unit cell wall (edge 11). The pseudo-diffusion algorithm is illustrated in (c), with $k = 5$. $M(i, t)$ is set to 1 at the time t indicated by the numbers in the figure. The vertices (●) belong to the connected component containing v_5. The vertices (○) remain at $M = 0$ and thus belong to another connected component.

the faces are translated far away one from another; since the faces do not intersect anymore, they are not neighbours and thus they do not bound a solid cube anymore. A more subtle example is the initial cube, but with one face suppressed; here again, the remaining five faces do not bound a solid block. The following development is meant to address all these cases.

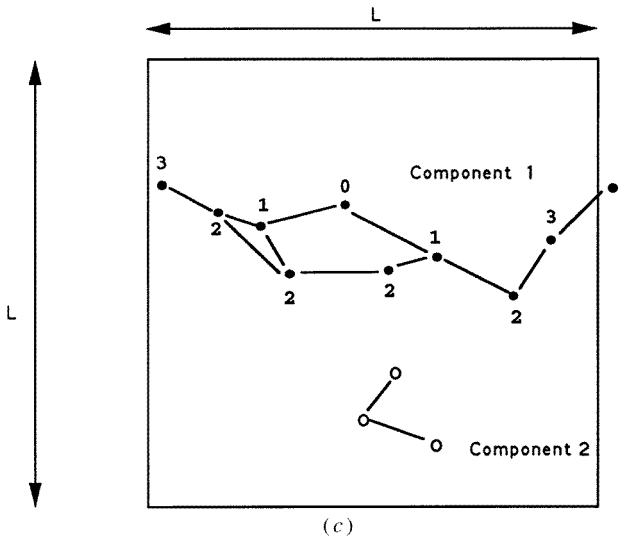

Figure 4. (Continued)

3.2.1. Elementary areas of the polygons. Elementary areas of the polygons are defined as the areas bounded by polygon edges and fractures intersections (cf figure 5); note that the elementary areas need not be simply connected, as A_2 in figure 5(b). An elementary face of a polygon is defined as an elementary area together with an oriented normal vector $\boldsymbol{n}$ to the polygon plane Π; the orientation is used to distinguish the two opposite sides of a fracture.

In order to find these areas, define the graph denoted by Γ_p, which consists of n vertices $V\Gamma_p = \{v_i, i = 1, 2, \ldots, n\}$ and m edges $E\Gamma_p = \{e_j; j = 1, 2, \ldots, m\}$. The vertices of Γ_p are given by the polygon vertices, the intersection end points, and the points where two intersection lines intersect inside the polygon. Then, oriented edges, denoted as e_j^{kl}, where the superscript kl indicates that the edge is oriented from vertex k to vertex l, are defined using an arbitrary orientation. The graph Γ_p is simple since only one edge connects two vertices, and no vertex is connected to itself, but the graph is not necessarily connected.

The first step towards finding the elementary areas of a polygon, is to reduce the graph Γ_p to a graph Γ'_p without dangling ends. All the edges which connect a vertex v_m to only one vertex v_n, are removed. This procedure is repeated until no progress can be made anymore and the result is displayed in figure 5(b). In the next step, all the connected components of Γ'_p are identified. In figure 5(b), the graph Γ'_p consists of two connected components, one made up by the vertices v_{21}, v_{22} and v_{23}, and their edges, and a second made up by the rest of the vertices and their edges. The components are identified using a graph diffusion algorithm, such as the one given by Prince (1994).

The elementary areas in a polygon are bounded by one or more *minimal cycles* of Γ'_p. As usual, a cycle of Γ'_p denotes a chain of vertices where the first and last vertex is the same. A minimal cycle is a cycle of Γ'_p which cannot be split into smaller cycles, such as the cycle defined by the vertices v_{21}, v_{22} and v_{23} in figure 5(b). As a counter example, consider the bounding edges of the whole polygon (i.e. v_1–v_2–$\cdots$–v_6) in the same figure, which do not constitute a minimal cycle, since this cycle contains other cycles of lesser extent. Note that our definition is a metric one, introduced to identify the smallest connected fracture areas.

In order to find the elementary areas, all the minimal cycles for each of the components

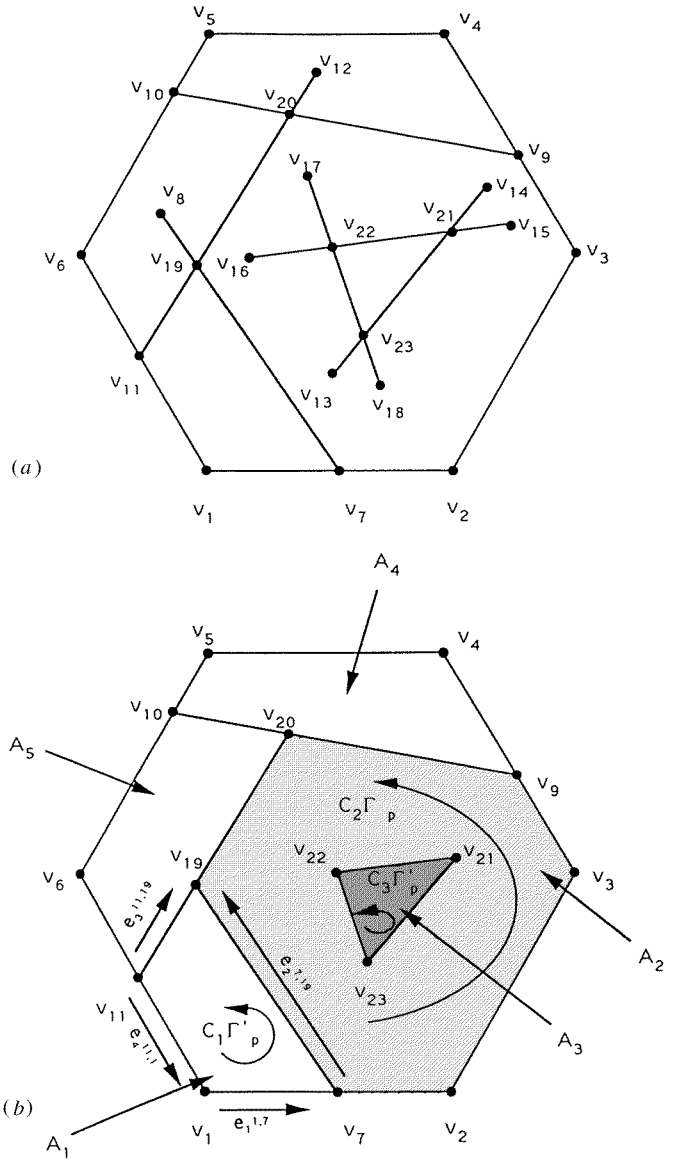

Figure 5. Elementary areas inside a fracture $(v_1, v_2, \ldots, v_6)$ in the fracture plane Π with normal vector $\boldsymbol{n}$. In (a), the graph Γ_p is composed by nodes which are polygon vertices, intersection vertices or points inside the polygon where two intersection lines intersect. The edges of Γ_p are parts of the polygon edges or intersection lines that connect the vertices. In (b), the graph Γ_p is reduced to Γ'_p without dangling ends; the elementary areas A_1 to A_5 bounded by the elementary cycles $C_i\Gamma'_p$ can be identified.

of Γ'_p are needed. This is done by walking along the edges and always turning to the same direction (right or left) at a vertex where two edges meet. In the course of this cycle identification, a positive direction is assigned to the cycles, i.e. they are oriented counter clockwise according to the normal vector with positive Z-coordinate of the polygon.

The orientation can be given in an edge vector notation $\boldsymbol{C}\Gamma'_p = \{d_j : j = 1, 2, \ldots, m\}$ where d_j is $+1$ if edge e_j^{kl} is visited from vertex k to vertex l, -1 if it is visited in the opposite direction and 0 otherwise. The oriented cycle $\boldsymbol{C}_1\Gamma'_p$ in figure 5(b) is denoted by $\{1, 1, -1, 1, 0, 0, \ldots, 0\}$.

The elementary areas are now given by the bounding minimal cycles. In figure 5(b) the area A_2 is given by $\boldsymbol{C}_2\Gamma'_p - \boldsymbol{C}_3\Gamma'_p$. Hence, it is necessary to determine the cycles which may lie inside other cycles. Cauchy's integral formula (Morse and Feshbach, 1953), valid for functions analytic on and inside a closed contour C

$$f(z_0) = \frac{1}{2\pi i}\int_C \frac{f(z)}{z - z_0}\,\mathrm{d}z \tag{2}$$

implies that if a point $\boldsymbol{p}$ lies in the interior of a closed contour C, the sum of the (oriented) angles α_i between $(\boldsymbol{v}_i - \boldsymbol{p})$ and $(\boldsymbol{v}_{i+1} - \boldsymbol{p})$ is 2π. The sum is zero if the point lies in the exterior of C.

The area bounded by one contour can be found using Green's theorem

$$\int_R\int \left(\frac{\partial Q}{\partial x} - \frac{\partial P}{\partial y}\right)\mathrm{d}x\,\mathrm{d}y = \int_C (P\,\mathrm{d}x + Q\,\mathrm{d}y) \tag{3}$$

where R is a simple connected area bounded by a cycle C. With $P = -y/2$ and $Q = x/2$, it yields

$$A = \int_R\int \mathrm{d}x\,\mathrm{d}y = \tfrac{1}{2}\int_C (x\,\mathrm{d}y - y\,\mathrm{d}x). \tag{4}$$

Now, the numerical value of each elementary area is given by the proper sum of contour integrals taken over the minimal cycles which bound it. For instance, the area A_2 in figure 5(b) is derived as

$$A_2 = \tfrac{1}{2}\int_{C_2\Gamma'_p} (x\,\mathrm{d}y - y\,\mathrm{d}x) - \tfrac{1}{2}\int_{C_3\Gamma'_p} (x\,\mathrm{d}y - y\,\mathrm{d}x). \tag{5}$$

3.2.2. Building of the fracture face graph Γ_2. Once the elementary areas have been identified for each polygon in the fracture network, the graph Γ_2 can be built and used later to find the blocks generated by the network. As mentioned above, the vertices $V\Gamma_2$ of Γ_2 correspond to the elementary areas of a polygon, together with a sign of the normal vector. The edges $E\Gamma_2$ of Γ_2, are set up between two vertices if the vertex pair satisfies one of the three following conditions.

The first possibility for two vertices to be connected, is sharing an original polygon edge. This occurs if two vertices v_i and v_j of Γ_2 are the two faces of the same elementary area, which has an original polygon edge in its bounding cycle. In figure 6, an example is provided by the two vertices, v_{12}^+ and v_{12}^- (in b) created by the same area A_{12}, (in a) with $+$ or $-$ denoting positive or negative normal vector. This area has one edge from the original polygon 1.

Second, two vertices v_i and v_j of Γ_2 are connected if they lie in the same plane and share an intersection edge where no other vertex connects. In figure 6, this is verified by the vertices v_{11}^+ and v_{12}^+ (in b) created from the elementary areas A_{11} and A_{12}, (in a) and both with normal vector $+\boldsymbol{n}_1$. This case occurs only for T-shaped intersections. This information is derived and stored when the networks are created.

Finally, two faces can be adjacent in a less trivial way which requires three tests. Consider figure 7(a), where four elementary areas of two plane polygons are drawn. The first obvious condition that has to be fulfilled by the two elementary faces denoted a_+ and

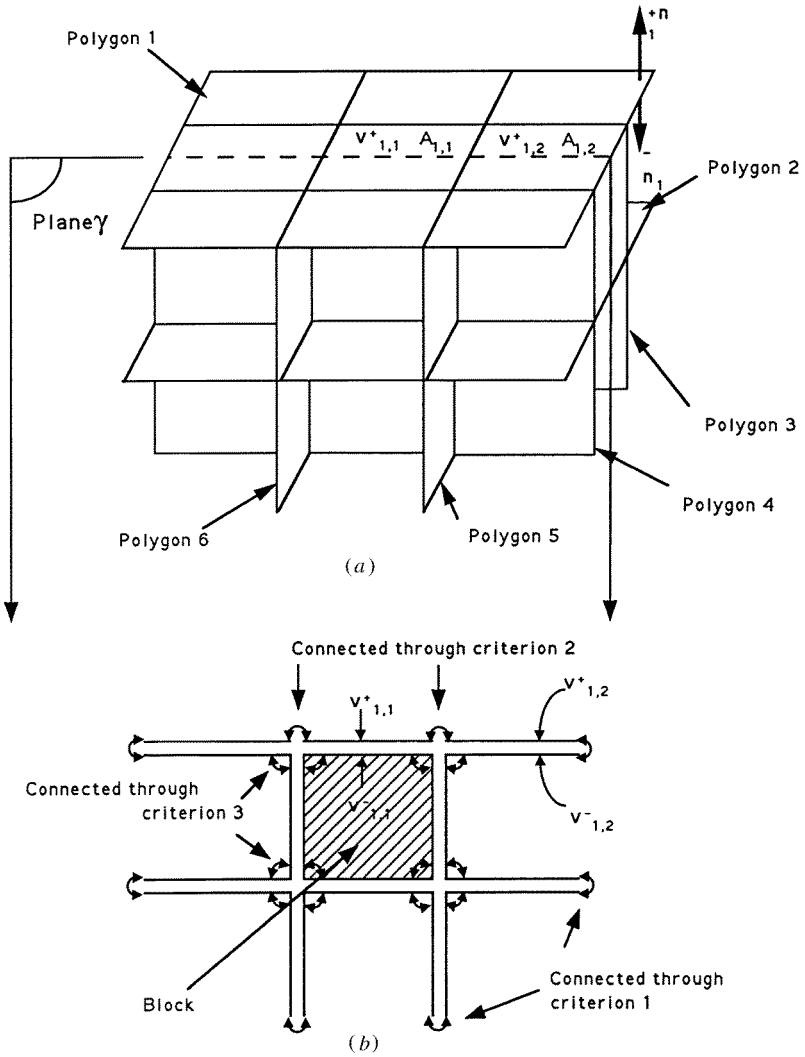

Figure 6. Adjacency criteria. (*b*) is the 2D cross-section of (*a*) in the plane γ. All the elementary areas, such as A_{11} and A_{12}, correspond to two vertices, one for the positive and one for the negative normal vector of the area.

b_+ is that the two faces must share an edge. Moreover, the vectors along the common edge oriented in the same way as the cycles bounding the faces, must point in opposite directions; hence,

$$-\nu_{a^+} = \nu_{b^+}. \tag{6}$$

The third condition requires that

$$(\boldsymbol{n}_{a^s} \times \boldsymbol{\nu}_{a^s}) \cdot \boldsymbol{n}_{b^s} \geqslant 0 \tag{7}$$

where s indicates the sign $\pm$.

This allows to distinguish the faces b^+ and c^-, which satisfy the two first criteria together with a^+. In figure 7(*b*), $\boldsymbol{n}_{a^+} \times \boldsymbol{\nu}_{a^+}$ and $\boldsymbol{n}_{b^+}$ point in the same direction, and the three conditions are fulfilled for the elementary faces a^+ and b^+.

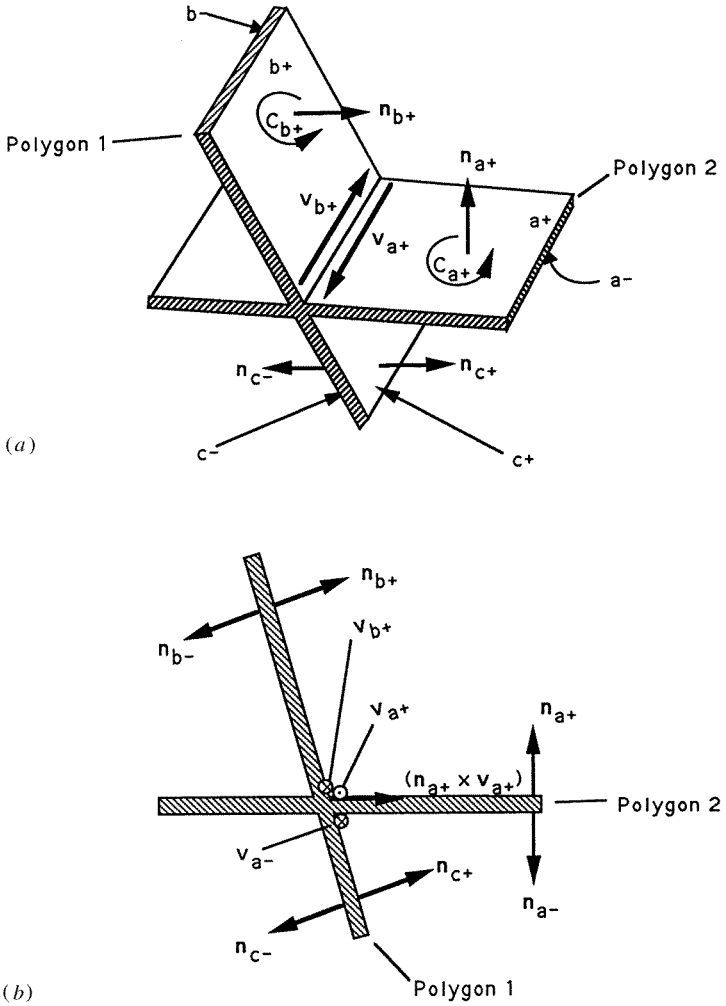

Figure 7. Illustration of the adjacency criterion 3. (*b*) is a vertical cross-section of (*a*). Four elementary areas from two polygons 1 and 2 are displayed, and three of them are denoted *a*, *b*, *c*. Each elementary area has two normal vectors associated with its two faces; for instance, *b* together with $\boldsymbol{n}_{b^+}$, defines the elementary face b^+. The cycles C_{b^+} and C_{a^+} are oriented counter clockwise around their respective normal vectors. $\boldsymbol{v}_{b^+}$ and $\boldsymbol{v}_{a^+}$ are vectors along the common edge of a^+ and b^+, oriented along their respective cycles. The vector $\boldsymbol{n}_{a^+} \times \boldsymbol{v}_{a^+}$ is displayed in (*b*); it points from the common edge of a^+ and b^+, into the elementary face a^+. $\boldsymbol{v}_{b^+}$ and $\boldsymbol{v}_{a^-}$ point into the plane ($\otimes$) whereas $\boldsymbol{v}_{a^-}$ points out of the plane ($\odot$). The elementary face b^+ is adjacent to a^+ because $\boldsymbol{v}_{b^+}$ and $\boldsymbol{v}_{a^+}$ point in opposite directions and $\boldsymbol{n}_{b^+} \cdot (\boldsymbol{n}_{a^+} \times \boldsymbol{v}_{a^+}) > 0$. No other elementary face in the figure is adjacent to a^+.

3.2.3. Identification of blocks created by fracture networks. The connected components of Γ_2 are identified using the same approach as described above for Γ_1. Blocks created in a fracture network generated from planar, finite-sized objects are in general complex geometrical forms which can be classified into two main groups. The first one consists of blocks bounded by finite connected components of Γ_2. Using Gauss' theorem (see e.g.

Adler, 1992), the volume enclosed by a component can be written as

$$\int_A \boldsymbol{r}\cdot\boldsymbol{n}\,\mathrm{d}A = \int_V \boldsymbol{\nabla}\cdot\boldsymbol{r}\,\mathrm{d}v = 3V = \sum_{i=1}^{n_k} \boldsymbol{r}_i\cdot\boldsymbol{n}_i A_i \tag{8}$$

where n_k is the number of vertices (elementary faces) in a component k, A_i is their area, $\boldsymbol{r}_i$ is a point in the face i and $\boldsymbol{n}_i$ its normal vector.

V derived by equation (8) is zero if the component does not surround any volume; in such a component, both faces of any elementary area are always present together, and with opposite normal vectors. The simplest example is provided by the two opposite faces of a single isolated fracture (see C_1 and C_2 in figure 8).

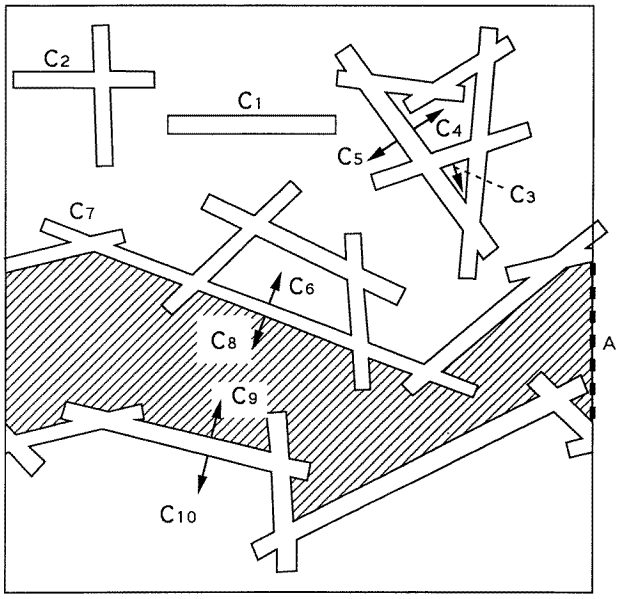

Figure 8. Volumes surrounded by the connected components of Γ_2. The components C_1 and C_2 have zero volumes. The components C_3, C_4 and C_6 enclose finite solid blocks. V derived from (8) is negative. C_5 encompasses C_3 and C_4, with V positive. The shaded area is an infinite block, bounded by C_8 and C_9. These components, together with the additional face A, enclose the fraction of the unit cell belonging to the infinite block.

If the volume, V, in equation (8) is not zero, the connected component actually surrounds a solid volume. Such components may also contain pairs of homologous faces, but these pairs do not contribute to the volume. V can be either positive or negative. A finite connected component surrounding a solid volume, like the inner envelopes C_3, C_4 or C_6 in figure 8, has always an outer counterpart, possibly infinite, which may encompass several disconnected solid volumes, like C_5 in the figure. As a consequence of the third criterion in section 3.2.3, the normal vectors of the inner envelopes are oriented inwards, and (8) yields a negative volume. Therefore, the finite solid blocks are identified with the finite connected components of Γ_2 for which (8) yields a negative volume.

The second group of blocks is unbounded. They are infinite but they can be characterized by their volume fraction within the unit cell. One way of doing this could be to supplement their envelope, which may consist of one or several infinite components of Γ_2, with faces along the boundaries of the unit cell (see figure 8). Equation (8) could then be applied to

the resulting finite connected component, and yield the volume of the infinite block within the unit cell.

A last special case occurs when a block lies inside another block. This situation is analogous in 2D to the area inside another area case for the elementary areas discussed above. To address this situation, the inner and outer blocks must be first determined. Afterwards, the volume is simply obtained by subtracting the volume of the inner block from the volume of the outer one. Note that the total number of blocks defined by a network is not affected by inner blocks. Two surfaces which define a large block containing an inner block, still define two blocks, as they would if the small one was located outside the large one. To decide whether or not a block B_1 lies inside another B_2, we first choose two points, one $\boldsymbol{p}_1$ on the surface of B_1, and one at infinity (e.g. randomly on a large sphere). Then, we move along a line defined from $\boldsymbol{p}_1$ to $\boldsymbol{p}_2$, and count how many times a surface of B_2 is crossed. If it is crossed an odd number of times, B_1 lies inside B_2.

4. Topology

4.1. Partition of the solid space by the fracture network

In this section, the partition of a solid space into blocks due to the existence of a fracture network is studied. As mentioned earlier, a fracture network divides the solid space into separated regions or blocks. Such a knowledge is important for several reasons. First, if flow and transport processes in a fractured porous media are considered, a two-scale problem can be set up, since flow occurs within the porous blocks themselves and through the fracture network. Second, another important application of block characterization is provided by the estimation of keyblocks in mechanical rock engineering. A keyblock is defined as a finite, undeformable block which can be translated towards (open) space without displacing adjacent rock, i.e. a removable block (Mauldon, 1995).

The number, N_b, of finite blocks in a fracture network depends upon the number density of fractures, as well as the orientations, sizes and shapes of the fractures. It has been studied in a systematic way for systems of equal-sized regular polygons.

N_b was calculated as a function of the fracture number density, $\rho = N_{fr}/L^3$, for squares and hexagons with a cell size $L = 2.5D$ and for octagons with $L = 2D$ (the fracture diameter $D = 2R$ is taken as length unit, i.e. ρ is the number of fractures per volume D^3). The average number of created blocks, N_b or the density of blocks $\rho_b = N_b/L^{-3}$ and its standard deviation $\sigma(\rho_b)$ were measured on 80 realizations for each fracture density. The results are displayed in figure 9(a). As expected, N_b increases with ρ. A regression analysis of $\ln(\rho_b)$ versus $\ln(\rho)$ yields

$$\rho_b = k\rho^{\alpha} \tag{9}$$

where the exponent α varies between 3.5 and 3.9. For identical fracture densities, polygons with a larger number of vertices N_v, always yield a larger block density, even though the exponent in (9) decreases slightly with N_v.

The influence of the fracture shape was further investigated by extending the range of N_v, for fixed values of the fracture density. N_b was simulated as a function of the number N_v, of polygon edges for regular triangles, squares, pentagons, hexagons, octagons, 12-gons and 16-gons. This was done for $L = 2D$ with $N_{fr} = 56$, 72 and 96 fractures, or number densities $\rho = 7$, 9 and 12. The results are displayed in figure 9(b). They are based on 100 realizations for each polygon-type and density. The density of blocks is again seen to increase as N_v increases; it tends towards a limit as the polygons become more and more circular.

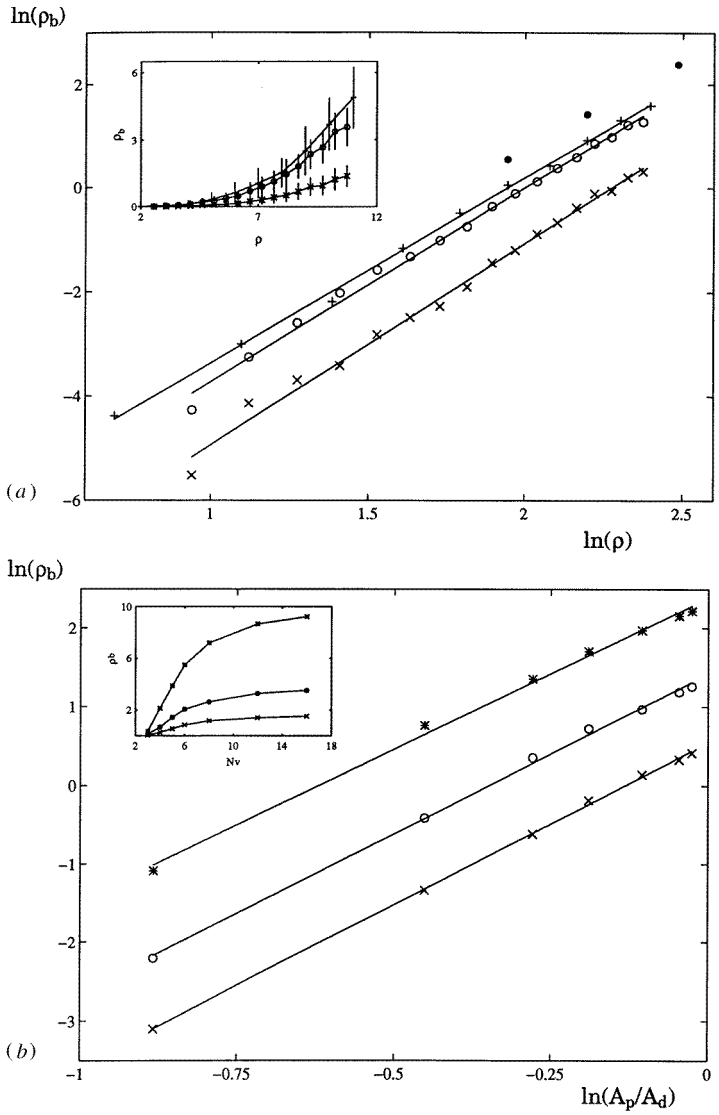

Figure 9. (*a*) Density of blocks in a fracture network, ρ_b versus number density of fractures ρ for equal-sized hexagons (○), squares (×) and octagons (+). The insert shows the results on a linear scale, whereas the results on log–log scale are given in the large figure. The straight lines in the log–log plot are the power-law fits (9). The circular limits (●) are obtained from equation (11). (*b*) Density of blocks ρ_b in fracture networks created by regular polygons with N_v edges, for three different fracture densities $\rho = 7$ (×), 9 (○), and 12 (∗). The small figure shows that ρ_b tends to a limit as $N_v \to \infty$, or equivalently as the polygon shape tends towards a circular disk. In the large figure, ρ_b is plotted versus the reduced polygon area A_p/A_d, on a log–log scale. The straight lines are the scaling law (11).

This dependency of ρ_b upon N_v can be investigated further by taking into account the area of the regular polygon A_p which may be expressed as

$$A_p = \tfrac{1}{2}R^2 N_v \sin\left(\frac{2\pi}{N_v}\right) = \frac{N_v}{2\pi}\sin\left(\frac{2\pi}{N_v}\right) A_d \tag{10}$$

where R is the radius of the circumventing disk and A_d its area. The log–log plot of ρ_b as a function of A_p/A_d in figure 9(b) yields an approximate straight line, with scaling exponents $\beta = 4.124$, 4.064 and 3.846 and correlation coefficients 0.9997, 0.9991 and 0.9983 for the three densities $\rho = 7$, 9 and 12, respectively. Thus, the number of blocks follows the approximate scaling law

$$\rho_b \propto \left(\frac{N_v}{2\pi}\sin\left(\frac{2\pi}{N_v}\right)\right)^{\beta} = \left(\frac{A_p}{A_d}\right)^{\beta} \tag{11}$$

with $\beta \approx 4$. In the limit of circular fractures ($Nv \to \infty$, $A_p/A_d \to 1$), these fits yield $\rho_b = 1.73$, 4.13 and 10.9 for $\rho = 7$, 9 and 12, respectively. In turn, this gives $\alpha = 3.41$, $k = 0.002\,26$ and $r = 0.999\,97$ in equation (9).

The formation of a polyhedron requires the intersection of a few fractures. The intersection of N independent surfaces is likely to be proportional to the product of their area. Since the tetrahedron is the polyhedron with the smallest number of faces, the number of tetrahedron should simply be proportional to A_p^4, in agreement with (11).

Furthermore, for moderate fracture density, one might expect the number of quadruplets of mutually intersecting fractures to scale as ρ^4. However, the exponent α in equation (9) depends on the fracture shape. This can be rationalized as follows.

Balberg *et al* (1984) introduced the so-called excluded volume, $V_{\rm ex}$, to quantify the average number N_I of intersections per object in a continuous system. Since ρ is the number of fracture per volume D^3,

$$N_I = \rho\frac{V_{\rm ex}}{D^3}. \tag{12}$$

Accordingly, the density ρ_I of the fracture intersections is

$$\rho_I = \rho^2\frac{V_{\rm ex}}{D^3}. \tag{13}$$

Let the density ρ' (and similarly $\rho'_b, \rho'_I, \ldots$) be the number of fracture per volume $V_{\rm ex}$

$$\rho' = \rho\frac{V_{\rm ex}}{D^3}. \tag{14}$$

Then

$$\rho'_I = \rho'^2. \tag{15}$$

For moderate fracture densities, one may infer the densities ρ'_T of triplets and ρ'_Q of quadruplets of mutually intersecting fractures

$$\rho'_T \propto \rho'^3 \qquad \rho'_Q \propto \rho'^4. \tag{16}$$

These relations hold for any fracture shape because this feature has been accounted for, through $V_{\rm ex}$, in the definition of the density ρ'.

All the data from figures 9(a) and (b) are recast in these terms in figure 10. $V_{\rm ex}$ for polygons was modelled as (Sahimi, 1995)

$$V_{\rm ex} = \tfrac{1}{2}A_pP_p \tag{17}$$

where P_p is the polygon perimeter. All the data collapse onto a single master curve, which is fitted by the power law

$$\rho'_b = 482\times10^{-6}\rho'^{3.79} \qquad r = 0.996. \tag{18}$$

The exponent 3.79 is indeed very close to the exponent 4 for ρ'_Q. This means that the model (17) for $V_{\rm ex}$ is successful not only to unify the density ρ'_Q for all particle shapes, but also

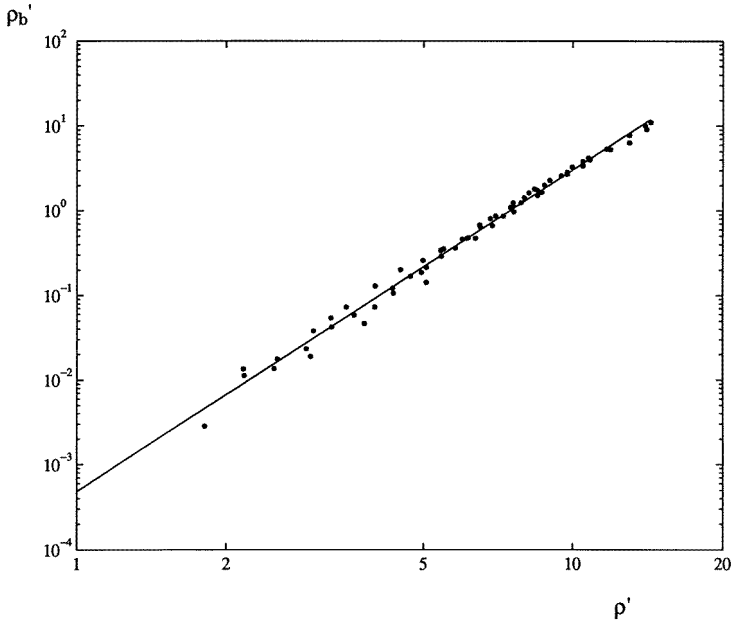

Figure 10. Block density ρ_b' versus fracture density ρ' for regular polygons with 3–16 vertices. The line is the least square fit (18).

to render the probability of a quadruplet of mutually intersecting fractures to form a closed block independent of the fracture shape.

Finally, it might be interesting to quantify the volume density of finite blocks, i.e. their volume fraction f_b. This parameter could prove useful for rock-mechanical purposes, for example as a damage index. Some results are presented in figure 11 for regular octagons in a cell with $L = 2D$. Clearly, two regions can be distinguished. For low fracture densities, a power-law relates ρ' and f_b. A least square fit yields

$$f_b = 49 \times 10^{-6}\rho'^{3.10} \qquad r = 0.98,\ \rho' \leqslant 10,\ f_b \leqslant 0.1. \tag{19a}$$

The initial growth of f_b is roughly cubic. Then, a transition occurs and f_b is a linear function of ρ'

$$f_b = -0.20 + 0.0272\rho' \qquad r = 0.999,\ 10 \leqslant \rho' \leqslant 14,\ 0.1 \leqslant f_b \leqslant 0.21. \tag{19b}$$

Ultimately, f_b is expected to reach one for a finite fracture density.

4.2. Topology of the fracture space

4.2.1. Percolation through a random fracture network. The percolating properties of a random fracture network are important for the transport properties. If the network does not percolate, the network permeability is necessarily equal to zero. Moreover, close to the percolation threshold, permeability is likely to obey universal power laws.

General. A review of continuum percolation is given by Balberg (1987), where important concepts such as V_{ex} are discussed. In Berkowitz (1995) and Berkowitz and Balberg (1993), application of percolation theory to fracture networks is reviewed.

For site or bond percolation on lattice systems, the main parameter is the probability p that a site is occupied, or a bond open. For continuum systems, where no lattice is involved,

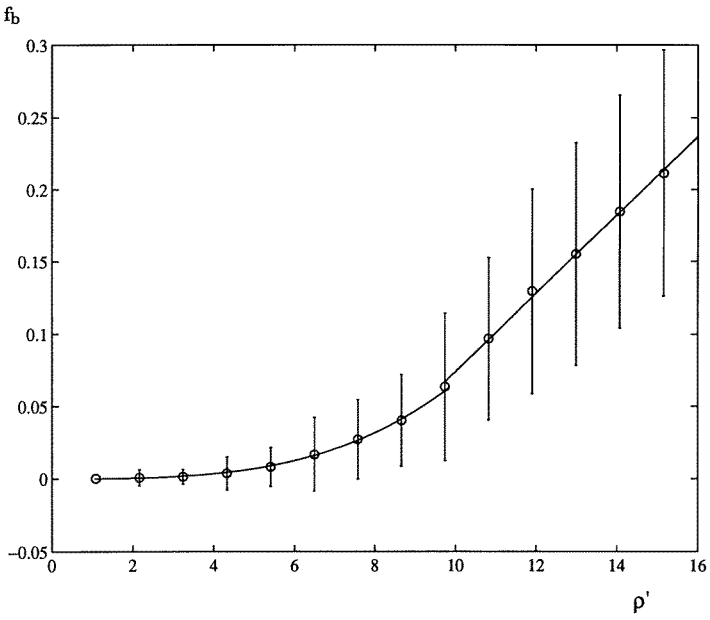

Figure 11. Volume fraction f_b of finite blocks in a network of octagonal fractures versus fracture density ρ'. The curves are the least square fits (19*a*) and (19*b*).

another parameter is usually used instead of the occupation probability, namely the number, N_I, of intersections, or bonds, per object. As a trivial consequence of (12) and (14),

$$N_I = \rho'. \tag{20}$$

Using continuum percolation simulations for various particle shapes, Balberg *et al* (1984) and Balberg (1985) established general percolation threshold criteria for 2D and 3D systems. They are valid for isotropic systems consisting of convex overlapping objects and read as

$$\begin{aligned} &3.2 < \rho_c' < 4.5 \qquad \text{(2D)} \\ &0.7 < \rho_c' < 2.8 \qquad \text{(3D)}. \end{aligned} \tag{21}$$

Later, our results will be discussed in view of these limits, and the expression of the V_{ex} of equal-sized disks is needed. In agreement with (17), it is given by Balberg (1987) as

$$V_{\text{ex}} = \pi^2 R^3. \tag{22}$$

To estimate the percolation thresholds for the random model described in section 2, the classical finite-size scaling method described in Stauffer and Aharony (1994) is used. The percolating system is studied for various cell sizes L. For given values of L and ρ, the probability $\Pi_L(\rho)$ of having a percolating cluster is derived from numerous realizations of the system. Then, the numerical function is used to estimate ρ_{Lc} (the value for which $\Pi_L(\rho) = \frac{1}{2}$) and an estimate of the width Δ_L of the transition region of $\Pi_L(\rho)$.

Once ρ_{Lc} and Δ_L have been evaluated for several values of L, the asymptotic value ρ_{Lc} for infinite systems ρ_c can be derived from the two scaling relations (Fischer, 1971, Charlaix, 1986)

$$\rho_{Lc} - \rho_c \propto L^{-1/v} \tag{23}$$

and

$$\Delta_L \propto L^{-1/\nu} \tag{24}$$

when $L \to \infty$.

In our estimations of ρ_{Lc} and Δ_L, the data for $\Pi_L(\rho)$ were fitted with an error function of the form (Stauffer and Aharony 1994, Reynolds *et al* 1980)

$$\Pi_L(\rho) = \frac{1}{\sqrt{2\pi}} \int_{-\infty}^{\rho} \frac{1}{\Delta_L} \exp\left\{ -\frac{(\xi - \rho_{Lc})^2}{2(\Delta_L)^2} \right\} \mathrm{d}\xi \tag{25}$$

where ρ_{Lc} and Δ_L are fit parameters.

Recall from section 3 that the method used to decide upon whether or not a percolating component is present in the fracture network, consists of first establishing the graph Γ_1 where the polygons are vertices, and where edges are set up if two polygons intersect. Then, a diffusion algorithm gives the connected and percolating components. A disadvantage of this method is the need of keeping the number of objects below the limits set by the computer memory. Also, the computer time increases proportionally to the square of the number of objects N, and this sets another limit on the tractable number of objects. Hence, N is fairly low, about 1200 for an IBM RISC 6000/220 with 32 Mbytes of internal memory. This is the reason why, in our calculations, L (measured in units of the disk diameter) was kept below 8. Despite the small cell sizes, the scaling laws (equations (23) and (24)) are well verified, which justifies the extrapolations of ρ_c at $L \to \infty$.

The polygons were created, and intersections identified as described in sections 2 and 3. Percolation was searched in all possible directions (x, y and z). Periodic boundary conditions were applied to the 3D graph during this search; this means that a cluster must touch two opposite faces of the unit cell, and in addition contain fractures intersecting one another across the faces.

Results. In the following, results obtained for regular equal-sized triangles, squares, hexagons, octagons, 20-gons and two sorts of rectangles are given. The rectangles have an aspect ratio $a/b = \frac{1}{2}$; the size of the first sort is constant, while the second one is inscribed within circles whose radii, R, are uniformly distributed between 0 and $R_{\max}$. Π_L is studied for four values of L for each polygon type, except for hexagons, where five L values were used.

An example of the plots of the estimated $\Pi_L(\rho)$ data points is given in figure 12, together with the fitted error functions. The trial form (25) of $\Pi_L(\rho)$ was found satisfactory in all cases. For the data in figure 12, the root mean square deviation of the numerical data from the fitted curves does not exceed 0.02 for all sample sizes. The uncertainties of the determinations of ρ_{Lc} and Δ_L are 0.02 and 0.03, respectively. Similar values apply for all polygon shapes. Plots of $\ln(\Delta_L)$ versus $\ln(L/D)$ were used to obtain the critical exponent ν; results and estimated errors are given in table 1. The various polygons are expected to belong to the same universality class, and ν was expected to be the same in all cases. The values were found in the range $\nu = 1.011 \pm 0.044$.

Plots of ρ_{Lc} versus Δ_L were extrapolated for $\Delta_L \to 0$ to find ρ_c, whose values are given in table 1, together with the linear correlation coefficients.

Discussion. Charlaix (1986) and Garborczi *et al* (1995) have obtained results for randomly distributed, equal-sized disks in 3D. In the latter reference, the disk results are available as the oblate limiting case of rotational ellipsoids. Since regular polygons were used rather than disks, our results need to be related to disk results, before a necessary comparison can be done.

If the values of ρ_c are compared for the various polygons, they seem to converge towards a limit as the number of vertices increases. This behaviour is made clear by the plot of ρ_c

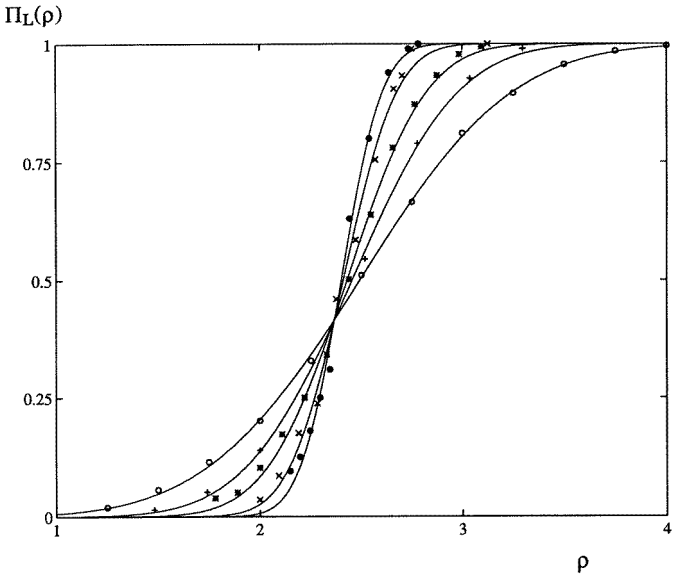

Figure 12. Probability of percolation versus number density of fractures in fracture networks created by equal sized, regular hexagons. The probability curves are simulated for sample sizes $L/D = 2$ (○), 3 (+), 4 (∗), 6 (×) and 8 (●). The full lines are the fitted error functions.

versus the ratio A_d/A_p (cf equation (10)) in figure 13. The linear relation which is obtained suggests that the circular disk limit can be obtained by extrapolating ρ_c for $A_d/A_p = 1$. For disks, this yields

$$\rho_c = 1.85 \pm 0.01. \tag{26}$$

Our results, as displayed in figure 13, fall between the estimations of Charlaix (1986) and Garborczi *et al* (1995), which are equal to 1.48 and 2.42, respectively.

This discrepancy requires some discussion. Garborczi *et al* (1995) did not use finite-size scaling methods. They used five realizations and recorded the number of particles at percolation. This is done for a system size which corresponds to $L/D = 20.8$. Therefore our results are not directly comparable with theirs, and this might explain the difference.

Charlaix (1986) used a finite scaling method, together with a larger span of system sizes than us, which should yield better estimates. However, our data plotted in figure 13 seem to be consistent, and to yield an unambiguous estimate for disks. Another point is that our definition of percolation involves the three possible directions, whereas Charlaix checked only in one direction. The two definitions are equivalent for infinite systems, and lower thresholds are expected in finite ones with our looser condition.

Our results can also be analysed in terms of the average number of intersections per fracture ρ'. The critical values ρ'_c deduced from ρ_c by equation (14) are listed in table 1. For regular polygons with N_v vertices, $V_{\rm ex}$ (17) may be expressed as

$$V_{\rm ex}/D^3 = \frac{\pi^2}{8}\left(\frac{N_v}{\pi}\right)^2 \cos\left(\frac{\pi}{N_v}\right)\sin^2\left(\frac{\pi}{N_v}\right). \tag{27}$$

For equal-sized rectangles with aspect ratio $\frac{1}{2}$, one obtains

$$V_{\rm ex}/D^3 = \frac{6}{5\sqrt{5}}. \tag{28a}$$

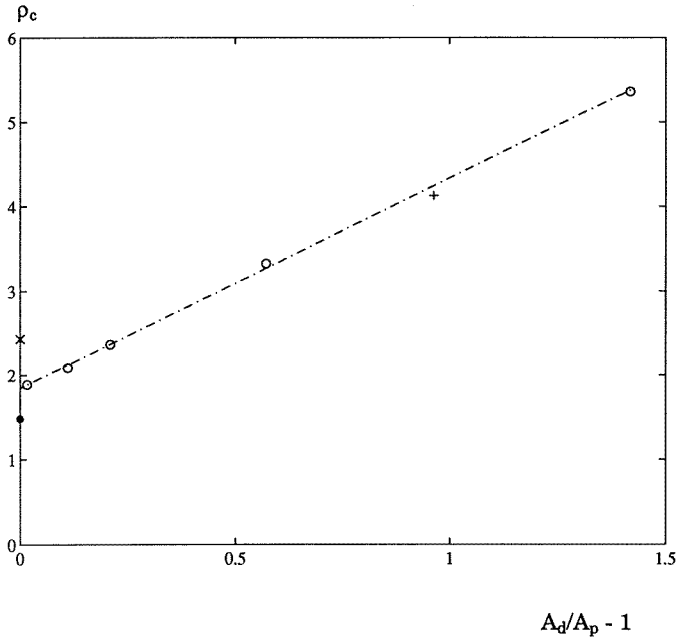

Figure 13. Percolation thresholds ρ_c for regular polygons (○) and rectangles with $a/b = 0.5$ (+) versus $(A_d/A_p - 1)$. The linear fit (— · —) yields $\rho_c = 1.846 \pm 0.015$ for disks. The data from Charlaix (1986) (●) and Garborczi *et al* (1995) (×) are given for a comparison.

For rectangles with aspect ratio $\frac{1}{2}$ and a size R uniformly distributed in $[0, R_{\max}]$, $V_{\rm ex}$ was averaged over the range of R, which yields

$$V_{\rm ex}/D^3 = \frac{3}{10\sqrt{5}}. \tag{28b}$$

The resulting values of ρ_c' listed in table 1 are remarkably constant. For all the fracture networks, including the cases of anisotropic (rectangular) and polydisperse polygons, ρ_c' lies in the range

$$\rho_c' = 2.26 \pm 0.04. \tag{29}$$

This result suggests to recast the data for ρ_{Lc} and Δ_L in a similar way. By analogy with (14), define

$$\rho_{LC}' = \frac{V_{\rm ex}}{D^3}\rho_{Lc}, \qquad \Delta_L' = \frac{V_{\rm ex}}{D^3}\Delta_L. \tag{30}$$

All the data can be recast in these terms in figure 14 and within deviations generally smaller than ±5% they can be gathered around a single curve. A linear fit yields the extrapolation

$$\rho_L' = 2.28 \qquad (L \to \infty). \tag{31}$$

In figure 14 which has been drawn at a large scale, small but systematic deviations occur; all data for triangles fall below, all data for squares above etc. Moreover, the deviations are smaller for larger N_v, when the polygon is close to a disk. The deviations are due to the approximate nature of $V_{\rm ex}$ in equation (17). Since our approximation gets better as the polygons approach circles, the points fall closer to the line for polygons with large N_v.

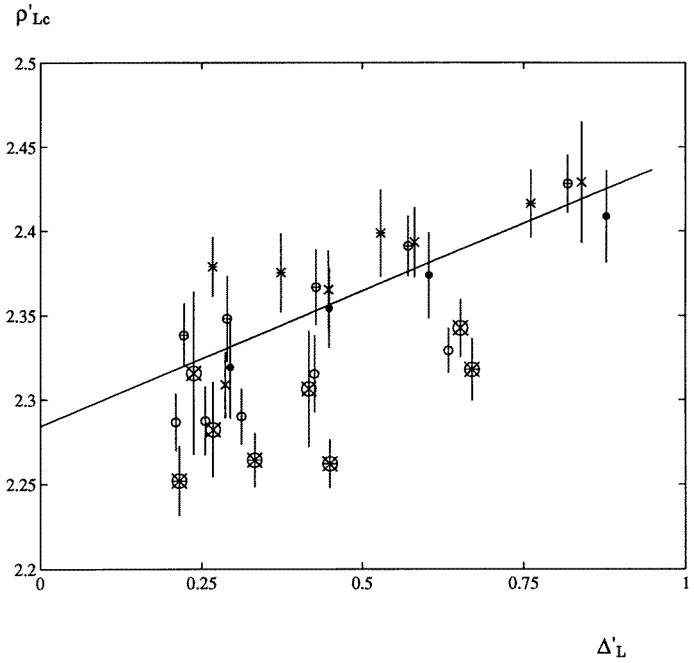

Figure 14. ρ'_{Lc} versus Δ'_L plotted for networks of triangles (○), squares (∗), hexagons (⊕), octagons (×) and 20-gons (●). The full line is a least square fit for the regular polygons. (⊛) are rectangles with aspect ratio $a/b = 0.5$; (⊗) are polydisperse rectangles with aspect ratio $a/b = 0.5$.

Nevertheless, the approximate formula for V_{ex} is quite successful for the regular polygons as well as for anisotropic and polydispersed ones.

In terms of ρ', the percolation thresholds obtained for disks by Charlaix (1986) and Garborczi *et al* (1995) are equal to $\rho'_c = 1.8$ and 3.0, respectively. Robinson (1983) obtained $\rho'_c = 2.09$ for the percolation of randomly centred unit squares oriented along three orthogonal directions.

Finally, note that our results agree with the limits set up by Balberg (1985) (equation (21)) for 3D systems. This is also true for the results obtained by Charlaix (1986), whereas the results from Garborczi *et al* fall outside these limits.

4.2.2. Betti numbers of fracture networks. The topological characterization of surfaces and solids has proven useful in various fields of physics, such as metallurgy and geological porous media. In the latter case, the 3D pore space has been characterized with the help of topological concepts by Thovert *et al* (1993), MacDonald *et al* (1986a, b) and by Lin and Cohen (1982) among others. The review of topology applied to metallurgy, written by Barret and Yust (1970), gives the main concepts and theorems useful for fracture networks.

The main topic addressed in this section is the determination of independent flow paths in fracture networks by using the topological information available from the graphs Γ_1 and Γ_2 defined and described in section 3. If flow paths in a fracture network can be described by curves connecting the centres of the fractures in a network, and if these curves connect all the centres of intersecting fractures, the physical situation is equivalent to the one introduced and used by Cacas *et al* (1990).

Because of its definition (cf section 3), Γ_1 can be used to find the independent flow paths of the fracture network. In view of this, some of the topological concepts described by Barret and Yust (1970) will be used; the zeroth Betti number $\beta_0(\Gamma)$ gives the number of connected components of a graph Γ. The first Betti number of a graph Γ is the number of independent cycles of the graph, and is given by the relation $\beta_1(\Gamma) = m(\Gamma) - n(\Gamma) + \beta_0(\Gamma)$, where $m(\Gamma)$ is the number of edges of Γ and $n(\Gamma)$ is the number of vertices of Γ. The first Betti number is also called the cyclomatic number or genus.

The two Betti numbers are readily obtained for the graph Γ_1. As explained in section 3, the connected components of Γ_1 are found using a pseudo diffusion routine; once they are identified, they can be counted, and the number of connected components gives $\beta_0(\Gamma_1)$. Since $n(\Gamma_1)$ and $m(\Gamma_1)$ are the number of vertices (polygons) and edges (intersections), the first Betti number of Γ_1 may be expressed as

$$\beta_1(\Gamma_1) = m(\Gamma_1) - n(\Gamma_1) + \beta_0(\Gamma_1). \tag{32}$$

The cyclomatic number of the graph Γ_1 is equal to the number of independent cycles. However, it can be argued that some of the cycles contributing to this sum do not correspond to physical flow cycles in a fracture network. To explain this, consider figure 15, where (*a*) and (*b*) display configurations with five intersecting fractures, and (*c*) and (*d*) the corresponding parts of Γ_1. If a point where three fractures intersect is denoted a *triple point*, the difference between (*a*) and (*b*) is that in (*a*) the fractures constitute a triple point whereas in (*b*) no triple point exists. Note that in graph Γ_1, the configurations (*a*) and (*b*) give the same structure, and that both configurations are therefore counted as a cycle. However, if a continuous deformation is considered (or *deformation retract*) of a curve circumventing the triple point in (*a*), and the punctured hole in (*b*), the curve can be deformed to a point in (*a*) but not in (*b*). This means that only case (*b*) corresponds to an actual flow cycle. Therefore, an alternative cyclomatic number $\gamma_1(\Gamma_1)$ is introduced, from which cycles corresponding to triple points are removed.

However, special care has to be taken with triple points involved in the bounding surfaces of blocks. Consider for example the tetrahedron block in figure 15(*e*). A cycle of three faces exists around each of four triple points, but these cycles are not independent, as shown by the corresponding graph in figure 15(*f*). More generally, a block with p vertices contains $p - 1$ independent cycles of Γ_1. Thus, the total contribution of the blocks to β_1 is their total number of vertices minus one per block. Accordingly, γ_1 is defined as

$$\gamma_1 = \beta_1 - N_T + N_b \tag{33}$$

where N_T is the number of triple points in the fracture network and N_b the number of blocks. This quantity, which models the number of independent flow paths in the network, is available when the number of polygons, intersections, triple points, blocks and connected components of Γ_1 are known.

Finally, volumetric cyclomatic numbers are defined by

$$\bar{\beta}_1 = \left(\frac{D}{L}\right)^3 \beta_1 \qquad \bar{\gamma}_1 = \left(\frac{D}{L}\right)^3 \gamma_1. \tag{34}$$

These parameters are intrinsic cycle densities, whereas β_1 and γ_1 are absolute number of cycles in the cell with size L.

Cyclomatic numbers as functions of polygon shape. The cyclomatic numbers β_0, $\beta_1(\Gamma_1)$ and $\gamma_1(\Gamma_1)$ were calculated as functions of the number N_v of vertices in regular polygons in

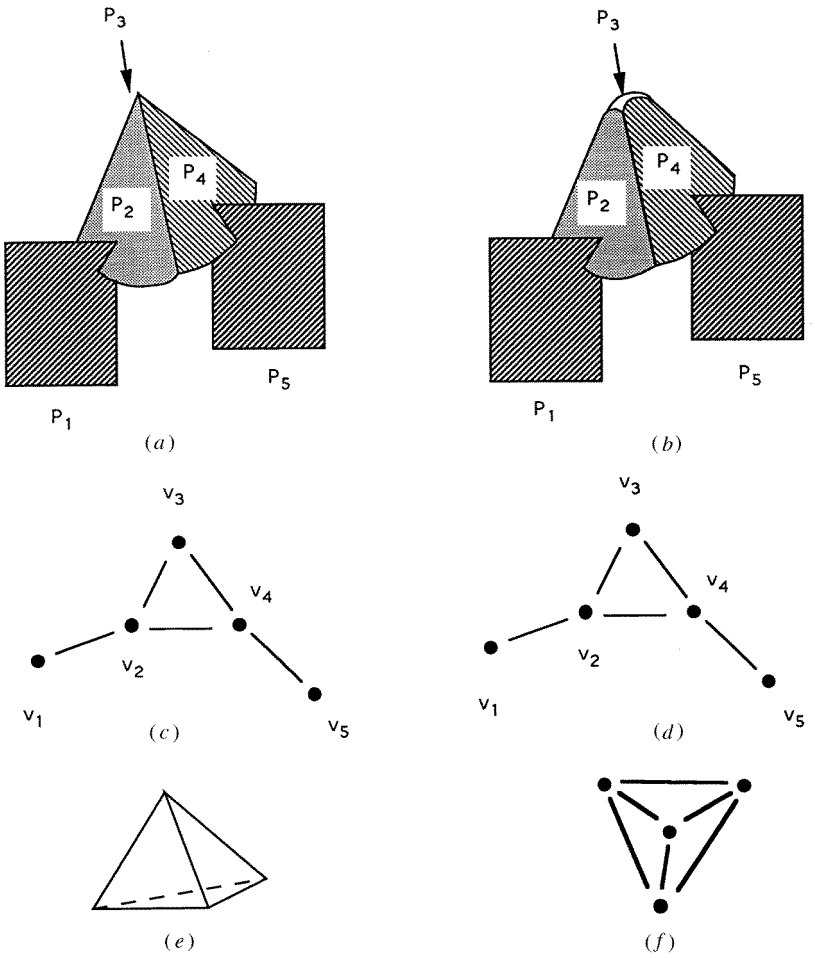

Figure 15. Two situations involving five fractures with (*a*) or without (*b*) triple points. The corresponding graphs are identical (*c*, *d*). Tetrahedric block (*e*) and its graph (*f*).

a cell of size $L = 2D$. Three number densities $\rho = 7$, 9 and 12 were used, corresponding to 56, 72 and 96 fractures. The results for $\bar{\beta}_1(\Gamma_1)$ and for $\bar{\gamma}_1(\Gamma_1)$ are displayed in figure 16 together with semi-analytic curves derived as follows. Qualitatively, $\bar{\beta}_1(\Gamma_1)$ and $\bar{\gamma}_1(\Gamma_1)$ are seen to converge towards a limit when N_v tends to infinity i.e. when the polygon shape becomes circular, as one should expect. Moreover, $\bar{\gamma}_1(\Gamma_1)$ converges much faster than $\beta_1(\Gamma_1)$.

Let us explain the behaviour of $\bar{\beta}_1(\Gamma_1)$ defined by (32). Since in Γ_1 fractures are replaced by vertices and intersections by edges, n is equal to the number of fractures in the network, i.e. $\rho L^3/D^3$. Now, the number of edges in Γ_1 is half the number of intersections per polygon times the number of polygons. Accordingly, $m(\Gamma_1)$ is given by $\frac{1}{2}\rho' n(\Gamma_1) = \frac{1}{2}\rho'\rho L^3/D^3$. Therefore, the cyclomatic number of the network may be expressed as

$$\beta_1(\Gamma_1) = \left(\frac{L}{D}\right)^3 \rho \left(\frac{\rho'}{2} - 1\right) + \beta_0. \tag{35}$$

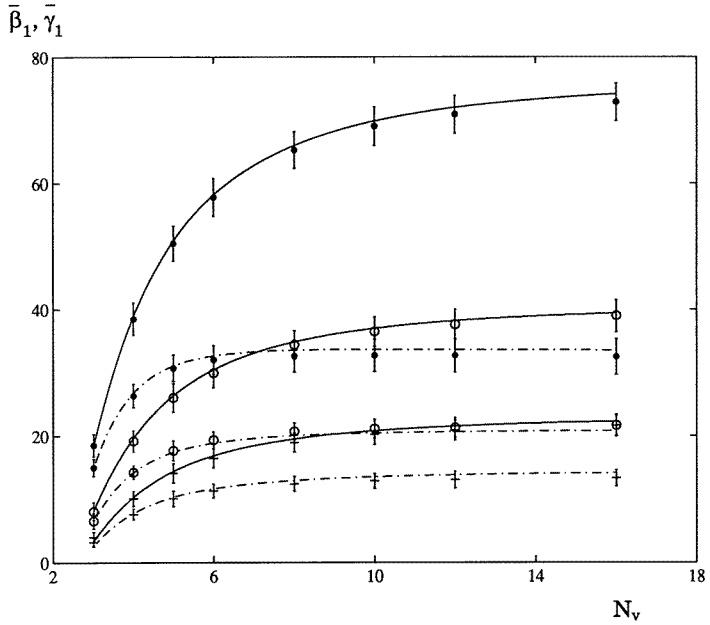

Figure 16. Volumetric cyclomatic numbers $\bar{\beta}_1$ (——) and $\bar{\gamma}_1$ (— · —) for networks of regular polygonal fractures with densities $\rho = 7$ (+), 9 (○) and 12 (●), as functions of the number of polygon vertices N_v. The curves are the predictions (36) and (38).

Since β_0 is small compared with β_1 when ρ is larger than 3, the cycle density $\bar{\beta}_1$ is given by

$$\bar{\beta}_1 = \left(\frac{\rho'}{2} - 1\right)\rho. \tag{36}$$

This theoretical prediction is plotted in figure 16 together with the numerical data. The model (17) was used again for V_{ex}, and it is as successful here as it was for predicting block numbers or percolation threshold.

Similar predictions can be established for γ_1, by using estimates of the numbers N_T of triple points and N_b of blocks which appear in equation (33). For a given fracture density, the density of blocks was found to obey the power law (11) with an exponent close to 4. This is again verified for the data, with prefactors 1.5, 3.5 and 9.10, exponents $\alpha_1 = 3.994$, 4.068 and 3.746, and correlation coefficients 0.9998, 0.9986 and 0.9986, for $\rho = 7$, 9 and 12, respectively.

Similarly, the number of triple points for a given density ρ is expected to scale as the cube of the fracture area. This was also checked on the data, which yield

$$\rho_T \propto \left(\frac{A_d}{A_p}\right)^{\beta_T} \tag{37}$$

with prefactors equal to 10.2, 21.8 and 52.9, exponents equal to 2.87, 2.96 and 2.97 and correlation coefficients equal to 0.9998, 0.9998 and 0.9999 for $\rho = 7$, 9 and 12, respectively.

Now, from (33) and (34), $\bar{\gamma}_1$ reads

$$\bar{\gamma}_1 = \bar{\beta}_1 - \rho_T + \rho_b. \tag{38}$$

The estimation of $\bar{\gamma}_1$ using (36) with (27) and the two fits above for ρ_T and ρ_b is plotted in figure 16. Again, an excellent agreement with the numerical data is observed.

Betti numbers versus number density of fractures. Finally, it is possible to recast the volumetric cyclomatic numbers as was done for the other densities (see (14))

$$\beta_1' = \frac{V_{ex}}{D^3}\bar{\beta}_1 \qquad \gamma_1' = \frac{V_{ex}}{D^3}\bar{\gamma}_1. \tag{39}$$

These quantities represent numbers of cycles in Γ_1 per excluded volume V_{ex}. Equivalently, from (33, 34, 36, 39)

$$\begin{aligned} \gamma_1' &= \left(\frac{\rho'}{2} - 1\right)\rho' - \rho_T' + \rho_b' \\ \beta_1' &= \left(\frac{\rho'}{2} - 1\right)\rho'. \end{aligned} \tag{40}$$

It was shown in the previous paragraphs that ρ_b' can be deduced from ρ' (see (18)). The triple point density ρ_T' could also be fitted by a power law in fair agreement with (16)

$$\rho_T' = 0.0117\rho'^{3.19} \qquad r = 0.9985. \tag{41}$$

Accordingly, (40) can be recast into

$$\gamma_1' = \left(\frac{\rho'}{2} - 1\right)\rho' - 0.0117\rho'^{3.19} + 482\,10^{-6}\rho'^{3.79}. \tag{42}$$

Hence, all the influence of the fracture geometry on the Betti numbers is accounted for through the volume V_{ex} in the definition of the densities. Only the two last terms of (42) are numerical fits (see figure 11).

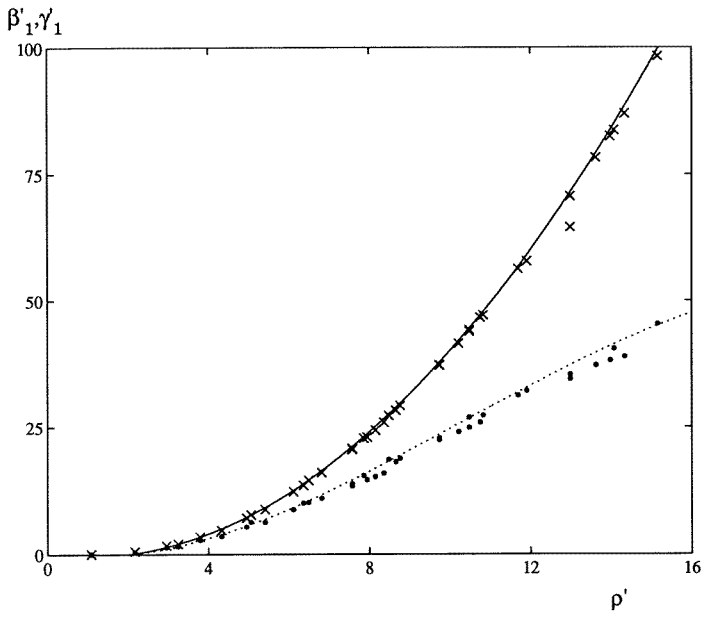

Figure 17. Volumetric cyclomatic numbers β_1' (×) and γ_1' (●) versus fracture density ρ' for networks of regular polygonal fractures with 3–16 vertices.

The predictions (40) and (42) are compared with the numerical data in figure 17. The agreement is again excellent, in particular for β_1', whose prediction (40) does not involve any adjustable parameter, apart from the definition (17) of the V_{ex}.

5. Conclusions

The most salient result of this work is probably the successful use of V_{ex} (17) to account for most of the influence of the fracture geometry, since it gathers all the results for the various quantities investigated in section 4. This can be summarized as follows. The finite-block density reads (see equation (18) and figure 10)

$$\rho_b' = 4.82 \times 10^{-6} \rho'^{3.79}.$$

The percolation threshold is (see table 1)

$$\rho_c' = 2.26 \pm 0.04.$$

The first Betti number is given by (see figure 17)

$$\beta_1' = \left(\frac{\rho'}{2} - 1\right) \rho'$$

$$\gamma_1' = \left(\frac{\rho'}{2} - 1\right) \rho' - 0.0117 \rho'^{3.19} + 482 \times 10^{-6} \rho'^{3.79}.$$

These results were shown to hold for equal-sized regular polygons, and also for ρ_c', β_1' and γ_1' for mono- and polydisperse rectangles with moderate aspect ratios.

Since natural fracture networks are likely to have more complex size and shape distributions, the definition (17) of V_{ex} should be checked and possibly improved for more general fracture populations. Of particular importance is the type of average to be performed when fractures with different sizes and/or shapes coexist in the network. The arithmetic average (28*b*) for polydisperse rectangles proved successful in the present case, but this might be fortuitous since it was not derived by any rigorous argument. For example, an alternative definition where the polygons areas and perimeters A_p and P_p are averaged prior to estimating the product (17) does not yield satisfactory results (e.g. $\rho_c' \approx 1.5$, much lower than $\rho_c' = 2.26$ for the monodisperse cases).

Acknowledgments

One of us (OKH) thanks the Norwegian Research Council (NFR) for financial support. Most computations have been performed at CNUSC (subsidized by the MESR) whose support is gratefully acknowledged.

References

Acuna J A and Yortsos Y C 1995 Application of fractal geometry to the study of networks of fractures and their pressure transient *Water Resours. Res.* **31** 527–40

Adler P M 1992 *Porous Media* (Stoneham, MA: Butterworth-Heinemann)

Andersson J and Dverstorp B 1987 *Water Resours. Res.* **23** 1876–87

Balberg I 1985 'Universal' percolation-threshold limits in the continuum *Phys. Rev.* B **31** 4053–5

——1987 Recent developments in continuum percolation *Phil. Mag.* B **56** 991–1003

Balberg I, Anderson C H, Alexander S and Wagner N 1984 Excluded volume and its relation to the onset of percolation *Phys. Rev.* B **30** 3933–43

Barret L K and Yust C S 1970 Some fundamental ideas in topology and their application to problems in metallography *Metallography* **3** 1–33

Barthelemy P 1992 Etude de la géométrie des réseaux de fractures naturelles à différentes échelles *PhD Thesis* University Paris-Sud d'Orsay

Bear J, Tsang C-F and de Marsily G 1993 *Flow and contaminant transport in fractured rock* (New York: Academic)

Berkowitz B 1995 Analysis of fracture network connectivity using percolation theory *Math. Geol.* **27** 467–75

Berkowitz B and Balberg I 1993 Percolation theory and its application to groundwater hydrology *Water Resours. Res.* **29** 775–94

Billaux D, Chiles J P, Hestir K and Long J 1989 Three-dimensional statistical modelling of a fractured rock mass—an example from the Fanay-Augères mine *Int. J. Rock Mech. Min. Sci. & Geomech. Abstr.* **26** 281–99

Cacas M C, Ledoux E, de Marsily G, Tillie B, Barbreau A, Durand E, Feuga B and Peaudecerf P 1990 Modeling fracture flow with a stochastic discrete fracture network: calibration and validation. 1. The Flow Model *Water Resours. Res.* **26** 479–89

Charlaix E 1986 Percolation threshold of a random array of discs: a numerical simulation *J. Phys. A: Math. Gen.* **19** L533–6

Chiles J P 1988 Fractal and geostatistical methods for modeling of a fracture network *Mathematical Geology* **20** 631–54

Conrad F and Jacquin C 1975 *Representation of a Two-dimensional Fracture Network by a Probabilistic Model: Application to Calculation of the Geometric Magnitudes of Matrix Blocks* UCRL-TRANS, 10814

Cowie P A, Knipe R J and Main I G 1996 Scaling laws for fault and fracture populations. Analyses and Applications *Special Issue of J. Structural Geology* **18** 2, 3

Dershowitz W S and Einstein H H 1988 Characterizing rock joint geometry with joint system models *Rock Mech. & Rock Eng.* **21** 21–51

Fischer M E 1971 *The theory of critical point singularities* ed M S Green Critical Phenomena, Proc. 51st Fermi School, Varenna, Italy (London: Academic)

Garborczi E J, Snyder K A, Douglas J F and Thorpe M F 1995 Geometrical percolation threshold of overlapping ellipsoids *Phys. Rev.* E **52** 819–28

Genter A and Traineau H 1992 Preliminary geological results from granite core analyses for hot dry rock research *Scientific Drilling* **3** 205–14

Gertsch L S 1995 Three-dimensional fracture network models from laboratory-scale rock samples *Int. J. Rock Mech. Min. Sci. & Geomech. Abstr.* **32** 85–91

Lee J S, Veneziano B and Einstein H H 1990 *Rock Mechanics Contributions and Challenges* ed W A Hustrulid and G A Johnson (Rotterdam: Balkema) 261–8

Lin C and Cohen M H 1982 Quantitative methods for microgeometric modeling *J. Appl. Phys.* **53** 4152–65

MacDonald I F, Kaufmann P M and Dullien F A L 1986a Quantitative image analysis of finite porous media I. Development of genus and pore map software *J. Microsc.* **144** 277–96

—— 1986b Quantitative image analysis of finite porous media. II. Specific genus of cubic lattice models and Berea sandstone *J. Microsc.* **144** 297–316

Mauldon M 1995 Keyblock probabilities and size distributions: a first model for impersistent 2-D fractures *Int. J. Rock Mech. Min. Sci. & Geomech. Abstr.* **32** 575–83

Morse P M and Feshbach H 1953 *Methods of Theoretical Physics* part I (New York: McGraw-Hill)

Pollard D D 1976 On the form and stability of open hydraulic fractures in the earth's crust *Geophys. Res. Lett.* **3** 513–6

Prince C 1994 *Algorithmes de Graphes* Editions Eyrolles

Reynolds P J, Stanley H E and Klein W 1980 Large-cell Monte Carlo renormalization group for percolation *Phys. Rev.* B **21** 1223–45

Sahimi M 1995 *Flow and Transports in Porous Media and Fractured Rock* (Weinheim: VCH)

Sahimi M and Yortsos T L 1990 *Applications of Fractal Geometry to Porous Media: A review* Society of Petroleum Engineers, Paper 20 476

Stauffer D and Aharony A 1994 *Percolation Theory* 2 (London: Taylor and Francis)

Thovert J-F, Salles J and Adler P M 1993 Computerized characterization of the geometry of real porous media: their discretization, analysis and interpretation *J. Microsc.* **170** 65–79